TUDelft

Delft University of Technology

Seismic interferometry as a tool for improved imaging of the heterogeneities in the body of a landfill

Konstantaki, LA; Draganov, DS; Ghose, R; Heimovaara, TJ

Important note
To cite this publication, please use the final published version (if applicable).
Please check the document version above.

Seismic interferometry as a tool for improved imaging of the heterogeneities in the body of a landfill.

L. A. Konstantaki[a], D. Draganov[b], R. Ghose[b], T. Heimovaara[a]

[a]Section of Geoengineering, Dept. of Geoscience and Engineering, Delft University of Technology, The Netherlands.

E-mail: l.a.konstantaki@tudelft.nl; t.j.heimovaara@tudelft.nl.

[b]Section of Applied Geophysics and Petrophysics, Dept. of Geoscience and Engineering, Delft University of Technology, The Netherlands.

E-mail: d.s.draganov@tudelft.nl; r.ghose@tudelft.nl.

Corresponding author:

L.A. (Laura) Konstantaki

E-mail: l.a.konstantaki@tudelft.nl

Phone: +31 15 27 89132

Postal address: Stevinweg 1, PO-box 5048, 2628 CN Delft / 2600 GA Delft, The Netherlands.

ABSTRACT

It is challenging to image and characterize the body of a landfill. High-density areas that act as obstructions to fluid flow are of specific interest to the landfill operators (e.g., for improvement of treatment technologies), and thus their imaging is important. In seismic reflection sections, such areas manifest themselves as sources of scattered energy. The heterogeneities inside the landfill, in addition to the surface-wave energy which is difficult to remove, add to the complexity in the seismic data. We propose to make use of seismic interferometry (SI) as a tool to improve the imaging of the scatterers, but also as a tool to remove the undesired surface-wave energy. We investigate the results obtained from application of SI to field seismic reflection data recorded at a landfill. We show that the data, retrieved by SI, image the scattered energy better than the seismic reflection data when the latter is processed in a conventional way. The increased stacking power of SI and its implicit consideration of multiple scattering result in a better illumination of the scatterers. We also use SI to predict the surface-wave energy and remove it from the original seismic reflection data using an adaptive subtraction method. The result from the adaptive subtraction when compared to the reflection data, processed in a conventional way, shows improved imaging, especially of layers in the landfill. Combined interpretation of the stacked reflection sections together with the velocity fields obtained from the three different datasets (conventional seismic reflection, SI and adaptive subtraction) leads to an improved interpretation.

Keywords: Landfill seismic interferometry, heterogeneity, scatterers, adaptive subtraction, velocity analysis, surface waves.

1. INTRODUCTION

Using seismic interferometry (SI) it was previously shown that the imaging of near-surface (very shallow) scatterers in synthetic reflection seismic data was improved (Konstantaki et al., 2013). Compared to the data of conventional reflection seismic survey (CRSS), the results retrieved by SI were found to be less affected by errors that occur during data acquisition and processing, e.g., due to incorrect positioning of sources in time-lapse measurements or incorrect top muting. First goal of this research, is to test the previous numerical findings by applying SI to field reflection data recorded over a landfill. Both ambient-noise recordings (Campillo and Paul, 2003; Shapiro and Campillo, 2004; Draganov et al., 2007, 2009) and controlled-source recordings (Schuster, 2001; Wapenaar et al., 2002; Schuster et al., 2004) can be used in SI. Here we use controlled-source reflection recordings for SI.

In our application of SI, we cross-correlate common-receiver gathers recorded by two receivers – one at location A and another at location B – and then sum the correlation result along the sources with the aim of retrieving the reflection response at B from a virtual source at position A (e.g., Wapenaar and Fokkema, 2006; Wapenaar et al., 2010a). For a correct retrieval of the reflection response, the sources must surround the receivers. Nevertheless, it was found that even with sources and receivers only at the surface (as is the case for seismic reflection data acquisition on a landfill), the reflection response could still be retrieved (van Wijk, 2006; Halliday et al., 2007). In this case, however, non-physical arrivals might be retrieved as well (Snieder et al., 2006; Draganov et al., 2012; King and Curtis, 2012). Such non-physical arrivals would be suppressed when significant multiple scattering occurs in the subsurface (Wapenaar, 2006). In such cases, objects scattering seismic energy can be regarded as secondary (Huygens) sources that illuminate the receivers also from below.

Typically, a landfill is an extremely heterogeneous body which is full of localized objects responsible for scattered seismic energy in the reflection recordings. The presence of scattered energy in reflection data poses extra requirements to the acquisition and processing of data, thus making seismic imaging of landfills a challenging task. On the other hand, the presence of significant secondary scattering in the landfill makes the application of SI advantageous.

Backscattered or reflected body-wave seismic energy from the very near-surface objects is usually overlain by dispersive surface waves generated by an active source at the surface. Thus, an important challenge in imaging shallow scatterers through reflection seismics is the elimination of the surface waves. This is a difficult task.

Surface waves from other sources can also be recorded (e.g., anthropogenic traffic noise or noise from gas/water pipes in the subsurface) and interfere with the active recordings. More critically, the surface waves often have a similar velocity and frequency content to those of the investigated signal (reflections and scattering events), making it difficult to remove them by conventional methods like bandpass or frequency-wavenumber (f-k) filtering (Konstantaki et al., 2015). Slightly incorrect use of the parameters in the f-k filter may result in artifacts due to signal distortion and spatial correlation of the background noise thus lowering further the quality of an obtained image. In the synthetic data of Konstantaki et al. (2013), surface waves were not present. In field data, however, surface waves are usually present, and they typically obscure the imaging of the near-surface scatterers (Konstantaki et al., 2015). The second goal of our study is thus to investigate the use of SI for removal of surface-wave energy.

Prediction of surface waves with SI and their adaptive subtraction (AS) from the seismic reflection data is a way to remove the surface waves. SI can be used to predict surface waves without the need for a near-surface velocity model. After the prediction, the surface waves retrieved by SI can be subtracted from the original reflection data using an adaptive filter (Dong et al., 2006; Halliday et al., 2010). Halliday et al. (2010) specifically mention the difficulties of removing scattered surface-wave energy from the reflection data by conventional processing and show the advantages of AS after prediction with SI. We test the use of SI to predict the unwanted surface waves and remove them from the reflection data with the goal to improve the imaging of the landfill.

Reliable characterization and imaging of the heterogeneities inside a landfill is becoming increasingly important. Definition of the aftercare period, prediction of the emission potential, and improvement of the treatment technologies are lately important topics for the landfill operators. One of the goals is to minimize the aftercare period (e.g., Scharff, 2005; van Vossen, 2010). For that purpose, a good understanding of the processes occurring inside the landfill body (e.g., preferential flow paths, biogeochemical processes, settlement) is essential. Many of these processes depend strongly on the heterogeneity distribution inside the landfill. Konstantaki et al. (2015) proposed a new approach involving CRSS and electrical resistivity methods to image and characterize a landfill in detail. The third goal of this study is to investigate the possibility to improve the characterization of a landfill when interpreting together the results from the CRSS, SI and AS methods.

In the following sections, we discuss the application of SI to the CRSS data acquired at a very heterogeneous landfill site. We investigate if the causal part, the acausal part, or a combination of both parts of the retrieved wavefield from SI is best for the acquisition geometry that we have used. We compare the result of SI with that of CRSS. Next, we present the results after AS of surface waves as predicted by SI. Finally, we characterize the landfill by joint interpretation of the results of CRSS, SI and AS.

2. DATA ACQUISITION AND PROCESSING: CONVENTIONAL REFLECTION SEISMIC SURVEY

In the summer of 2013, we acquired CRSS data on a landfill in Wieringermeer, the Netherlands. We used 10-Hz horizontal-component geophones as receivers and a high-frequency, electrodynamic horizontal (shear-wave) vibrator as the source (Ghose et al., 1996; Brouwer et al., 1997; Ghose, 2012). The horizontal geophones are oriented in the crossline direction; the shear-wave vibrator is used in an SH mode, which is achieved by orienting it in the crossline direction as well. In such a way, we ensure that we generate and record SH waves. Compared to impulsive seismic sources, high-frequency vibrators are often more suitable for resolving the heterogeneities in a very heterogeneous shallow subsurface (e.g., Ghose et al., 1996; Ghose et al., 1998). We have used shear (S) waves because in low-velocity soft soils S waves generally offer higher resolution than P waves due to the much lower velocity for S waves, and more importantly because S-wave velocity is directly linked to the elastic rigidity of the subsoil and S waves are more sensitive to the subtle changes in the soil type (e.g., Ghose, 2003; Ghose and Goudswaard, 2004). We used 48 geophones planted along a straight line with a 0.5 m spacing between the geophones. We kept the geophone array fixed and moved only the source. We shot at 33 locations, starting 4 m before the first geophone and finishing 4.5 m after the last geophone using a source spacing of 1 m. The noise from the nearby gas pipes and the work at nearby industrial buildings resulted in a relatively low signal-to-noise (S/N) ratio in the data. Further details about the acquisition parameters together with a detailed description of the processing of the CRSS data can be found in Konstantaki et al. (2015).

The main processing steps we applied to the CRSS were as follows: (1) vibroseis source-signature deconvolution to compress the raw vibrograms for each shot seperately in order to correct for shot-to-shot variation (Ghose, 2002); (2) vertical stacking of shots at every source location; (3) bandpass filtering (4-10-160-200 Hz); (4) top, bottom and surgical muting for removing the unwanted surface waves; (5)

iterative velocity analysis; (6) normal moveout (NMO) correction and stacking; we also applied (7) prestack-depth migration.

3. PROCESSING FOR SEISMIC INTERFEROMETRY

3.1 Processing steps

To investigate if we can improve the results of CRSS at a landfill, we apply SI to the CRSS data. For this purpose, we perform the following steps. First, we compensate for intrinsic losses (dissipation) by multiplying the raw CRSS data by exp(1.3*t), where t is time. With this, we aim to boost the later arrivals for the correlation process. Then we top-mute the direct arrivals and sort the data to common-receiver gathers (CRG). After that, we cross-correlate the CRGs and sum each correlation result along the sources. As a final step, we apply a bandpass filter (5-35-95-110 Hz) to remove low- and high-frequency noise and a notch filter to remove the 50-Hertz powerline noise. The latter noise is present in the CRSS data, and the cross-correlation process amplifies it. Therefore, we need to suppress it. Once the virtual common-source gathers are retrieved by SI, we apply the same processing steps 4) to 6) as described in section 2. To obtain stacked images of the landfill from the SI data, we use retrieved common-midpoint (CMP) gathers with a CMP fold ≥ 6. We apply post-stack automatic gain correction (AGC) with a 30 ms window to the stacked images for a better visualization. We finally apply a post-stack bandpass filter (10-35-95-110 Hz) to remove the low- and high-frequency noise that is boosted by the correlation process. After the stacking, we perform a time-to-depth conversion using a smoothed version of the stacking velocity field.

3.2 Using parts of the causal and acausal retrieved results

Using SI by cross-correlation requires illumination from all sides. When the illumination is homogeneous, physical arrivals will be retrieved equally well in the causal and acausal part of the wavefield (Wapenaar, 2004; van Manen et al., 2005; Wapenaar et al., 2010b). The causal part refers to times later than the zero time (positive time) and the acausal part to times earlier than the zero time (negative time). In such a case, the final retrieved result can be taken only from the positive times, only from the negative times, or even from their summation, where the latter might result in improved S/N ratio. In case when the illumination is not homogeneous from all sides (e.g., when one-side illumination occurs or gaps in the illumination are present) then parts of the physical energy can be retrieved at positive times and other parts at negative times. Furthermore, artifacts may appear; for example, physical arrivals retrieved at negative

times may continue to positive times as non-physical arrivals and thus manifest themselves there as artifacts. For our dataset, the illumination is not homogeneous because the sources are present only at the level of the receivers instead of effectively surrounding the receivers. Therefore, to retrieve more complete reflections, we take parts of the positive times and/or parts of the negative times. To understand how we choose which parts to use, we make a simple assumption of a horizontally layered subsurface representing the landfill and a homogeneous halfspace below it (Figure 1). In the figure, the location of receiver A is the position where a virtual source will be retrieved, whereas location B is the receiver where we want to retrieve the reflection from the bottom of the layer. Using stationary-phase principles (Snieder, 2004) it can be shown that sources lying around the stationary-phase point (inside the stationary-phase region) contribute constructively to the retrieval of physical energy, while arrivals from sources outside this region interfere destructively. For our case with sources and receivers at the surface, a reflection is retrieved by the correlation, for example, of a primary reflection with its first-order free-surface multiple. The correlation process would subtract the traveltime of the primary from that of the multiple, resulting in the retrieval of a physical primary reflection between A and B. For the case in Figure 1 with a homogeneous horizontal layer, the stationary-phase point will be at a distance AB to the left of A or to the right of B. For a virtual source at A and a receiver at B, the reflection will be retrieved at positive times when the sources are located to the left of A (Figure 1a). Similarly, the reflection will be retrieved at negative times when all sources are present to the right of B (Figure 1b). Having a heterogeneous subsurface with scatterers will complicate the situation. In that case, such a simple analysis is not necessarily correct. The presence of scatterers in the subsurface partly helps to overcome one-side illumination as the scatterers act as secondary (Huygens) sources and energy is scattered back to the surface (e.g., Konstantaki et al., 2013). Nevertheless, the number and location of scatterers in the subsurface is unknown on beforehand and, hence, we do not know whether the secondary illumination would be sufficient to result in retrieval of physical arrival both at positive and negative times. If a physical arrival is retrieved only, for example, at positive times for a certain retrieved trace, summing to the positive times the retrieved negative times would not add extra information. For this reason, we inspect how the retrieved results look like for a number of virtual common-source gathers for positive times, negative times, summed times or a combination of all (mixed-traces approach).

From inspection, we conclude that for our field dataset we can decide which times (positive, negative or summed) to be used for each trace depending on the relative position of A, B, and the majority of sources. Instead of choosing the times for each trace of each virtual common-source gather separately, we make this procedure automatic. The general rule that we have applied is that we take positive times in case A is between B and the majority of sources and we take negative times when B is between A and the majority of sources. In order to make this distinction, we should have at least 2/3 of the sources on one side of A or B. With a total of 33 sources, it means that at least 22 sources must be on one side in order to consider them as acceptable majority. If that is not the case, then we take the summation of the retrieved positive and negative times to increase the S/N ratio. When A and B coincide, we take only the positive times. We can summarize this as follows:

$$trace = \begin{cases} Positive\ time, if\ q \geq 22\ with\ x^s < x^A < x^B\ ,or\ x^s > x^A > x^B\ ,or\ x^A = x^B \\ Negative\ time, if\ q \geq 22\ with\ x^s < x^B < x^A, or\ x^s > x^B > x^A \\ Sum\ of\ positive\ and\ negative\ time, if\ q < 22 \end{cases},$$

where x^s indicates the position of the sources, q is number of sources, x^A is the position of A and x^B is the position of B. A comparison among the SI mixed-traces approach (SI^M), the result when only the positive times are used (SI$^+$), the result when only the negative times are used (SI$^-$), and the CRSS data is shown in Figure 2. We choose the shot location at horizontal distance 7 m because it has a mixture of positive, negative and summed traces. The green rectangle shows the area of improvement in SI^M compared to SI$^+$. In the SI$^+$ result, the area enclosed by the green rectangle is ringy and events are difficult to interpret. Due to the ringy nature, the retrieved artifacts might be interpreted as scattering arrivals (e.g., the orange hyperbola). Retrieved artifacts are a result of non-homogeneous illumination. The artifact indicated with the orange hyperbola is a non-physical arrival due to insufficient illumination from the sources to the left of the virtual-receiver positions. We see here that the secondary scattering was not sufficient to overcome the problem of one-side illumination. To retrieve physical arrivals in this area, sources on the right side of the receiver locations must be used, which then corresponds to events retrieved at negative times (and/or summed times as explained in the equation above). Comparing SI^M with CRSS, we notice similarities between the events that are not clear in SI$^+$ (grey-shaded areas).

The red rectangles show the improvement in SI^M over SI$^-$. Note, for example, the retrieved events inside the right red rectangle which appear to propagate to the virtual

source. These are retrieved artifacts due to a lack of retrieved physical energy at that part of the negative times. The illumination from the sources located on the right of the virtual-receiver locations is insufficient. To retrieve physical arrivals in this area, sources on the left side of the receiver locations must be used, which then corresponds to events retrieved at positive times (and/or summed times as explained in the equation above).The grey-shaded areas and hyperbolas show a comparison between the three different SI results and the CRSS result for the reflections and the scattering events, respectively. The improvement of SI^M over SI^+ and over SI^- is clear – the events are more coherent and better identifiable in SI^M. The presence of sufficient scatterers might help to homogenize the illumination of the receivers from the active sources, and thus result in more comparable positive and negative times. For our data, we see that such homogenization is not the case due to the insufficient number of scatterers and the presence of intrinsic losses. Therefore, we need to use the mixed-traces approach.

The stacked sections from CRSS, SI^M, SI^+ and SI^- data (Figure 3) confirm our previous conclusions. Once again the rectangles mark the areas of improvement in the SI^M result compared to SI^+ and SI^- results, and the grey-shaded areas and hyperbolas mark the imaged scatterers to which the marked events shown in Figure 2 have contributed. In general, the events are more coherent in SI^M. They show more clarity and are in agreement with the CRSS result. The artifact highlighted by the orange hyperbola appears as a scatterer in the SI^+ result, whereas in the SI^M it can be interpreted as a linear event, similar to that in CRSS. In the red area marked in the SI^- result, it is visible that the S/N ratio is lower in SI^- than in SI^M. Because of these, from now onwards we will use only the SI^M result, but for simplicity we will call it just SI. Note that the ringing that appears in the lower left corner of the stacked images is an artifact of the post-stack bandpass filter. In Figures 3e-h we show enlarged areas from the stacks in Figures 3a-d, respectively, for better visualization of the scatterers.

4. IMAGING SCATTERERS WITH SEISMIC INTERFEROMETRY

4.1 Comparison of the results of SI and CRSS

Figure 4 presents an example of CRSS and SI common-source gather for a source at horizontal location 22 m. We show both raw (Figures 4a and 4c) and processed data (Figures 4b and 4d). We choose the common-source gather for a source at distance 22 m (thus different from the one in Figure 2), because both reflections and scattering events are easily interpretable here. Another reason is that we will subsequently use this shot gather in explaining AS for suppression of surface waves. The shot gathers in Figures 4b and 4d are obtained after application of the processing steps as explained

in section 2. The grey-shaded areas indicate interpreted reflections. Ideally, these events should be at the same position in all these plots. The red hyperbolas mark those scattering arrivals which we can identify on the CRSS shot gathers (Konstantaki et al., 2015), whereas the green hyperbolas mark the ones which we can interpret unambiguously only on the SI shot gathers and not on the CRSS shot gathers. As the CRSS data are obtained by deconvolution and the SI data by cross-correlation, both CRSS and SI data show traces with zero-phase wavelets. Scattering events 1 and 2 interpreted in the CRSS shot gather are also interpretable in the SI shot gather, though not equally clear. Scattering events 5 and 6 appear strongly in the SI data. There is a hint of their presence also in the CRSS gather, but there they are not unambiguous. Scattering events 3 and 4 apparently exhibit opposite polarities on the CRSS and SI gathers. This will be explained later on in section 4.2. The reflections are interpretable in both datasets, but in the SI gather they appear more continuous and coherent.

Figure 5 shows the stacked images obtained from the CRSS and SI datasets. Concentrating on Figures 5a and 5b, we can identify specific structures. Both sections show predominance of laterally continuous reflections on the right part (18 m to 26.25 m horizontal distance). A dome-like structure appears in the middle (approximately 13 m to 17 m horizontal distance), which is more prominent in the SI section. We shall explain this event further in the Discussion section, after having interpreted the results of the AS approach.

Looking carefully at the events in the SI and CRSS stacked sections, it is clear that more scatterers can be interpreted in the SI section. The interpreted scatterers are marked in Figures 5c and 5d. In Figures 5e-h we show enlarged areas from the stacks in Figures 5a-d, respectively, for better visualization of the scatterers. In accordance with the interpretations in the common-source gathers, the green colour indicates scatterers that can be interpreted only in the SI section but not in the CRSS section, whereas the red colour indicates scatterers that can be interpreted in the CRSS result. The blue arrows point to reflectors. The reflectors seen in the SI stacked section are interrupted by scatterers (e.g., scattering events 5 and 6 in Figure 5d), while in the CRSS section we do not see such interruption. The higher number of traces in the SI data has made it possible to distinguish these extra scatterers (Konstantaki et al., 2013). This will be further explained in section 4.3.

Shallow scatterers (e.g., green hyperbolas at a horizontal distance of about 9.25 m and 14.25 m, and two-way traveltimes (TWT) 25 ms and 30 ms, respectively) can be identified in the SI stacked section (Figure 5). In the CRSS section, these events are not interpretable, most likely because they were muted out in the preprocessing. In our

case, the SI data utilizes secondary scattering in order to retrieve the energy from the shallow scatterers and thus remedies the problem posed by muting in the CRSS data (Konstantaki et al., 2013).

4.2 Modelling study 1: Opposite-polarity effect

In Figure 5, we identify some events that exhibit opposite polarities between CRSS and SI stacked sections, similar to what we see in the shots gathers in Figure 4 (e.g., scattering events 3 and 4). Note that in the two stacked sections, scatterers 3 and 4 do not appear at the same location, although this was not apparent in the shot gathers in Figure 4. Concentrating on the events shown in the small yellow rectangles in Figure 5, we notice clearly the opposite-polarity effect: what appears to be a peak in the CRSS section (the red hyperbolas in the yellow rectangles in Figure 5c) shows up as a trough in the SI section (the red hyperbolas in the yellow rectangles in Figure 5d). A peak appears at an earlier time in the SI section (the green hyperbolas in the yellow rectangles in Figure 5d). These red- and green-marked events correspond to the same scatterer. We use Figure 6 to explain this effect. In Figure 6a the green hyperbola indicates a reflection event and the dashed green line is the same event after NMO correction. The blue hyperbola indicates a diffraction event and the dashed blue hyperbola is the alignment of the diffraction event after time-shifting using the root-mean-square (RMS) velocity of the reflection event for NMO correction. For velocity analysis, we use the stacking velocity corresponding to the main layer boundaries. The moveout velocity in this example is 90 m/s for the reflection and 60 m/s for the diffraction. When the reflection velocity field is used, the diffraction event is not flattened after the NMO correction (Figure 6a). This is true for both CRSS (Figure 6b) and SI (Figure 6c) data. However, as the SI data contain a larger number of traces (denser spatial sampling), it images the position of the scatterer more accurately. This can be interpreted as an aliasing effect in the CRSS result (due to spatial undersampling). As shown in Figure 6f, the stacked trace from the SI data provides a more correct time for the apex of the scatterer, compared to the stacked trace in the CRSS section (Figure 6e). In the CRSS stacked trace, we loose the information close to the apex and the scatterer appears at a later time. A comparison between the stacked traces shows a different waveform for the CRSS and SI result that could be interpreted as the opposite-polarity effect (grey arrows in Figure 6d), similar to what we observe in the field data (Figure 5).

4.3 Modelling study 2: Scatterers located at layer boundaries

To understand why the SI result could reveal scatterers that overlay reflectors, we perform a modelling study. We use a model consisting of four horizontal layers with two scatterers placed on the boundary between the two top layers (Figure 7a). The shear-wave velocity (V_s) and density (ρ) of the layers are: Layer1: V_s=82 m/s, ρ=800 kg/m^3; Layer 2: V_s=100 m/s, ρ=810 kg/m^3; Layer 3: V_s=120 m/s, ρ=820 kg/m^3; Layer 4: V_s=140 m/s, ρ=840 kg/m^3. Both scatterers are 1 m wide, 0.3 m high and have V_s=140 m/s and ρ=900 kg/m^3. The separation between the scatterers is 3 m. We consider the same acquisition geometry as we have in the field to generate synthetic data: 33 sources with 1 m spacing and 48 receivers with 0.5 m spacing. The first source is located at 134 m and the last source at 166 m, whereas the first receiver is located at 138 m and the last at 161.5 m. The scatterers are located at horizontal positions 148 m and 152 m. The grid sampling in the model is 0.09 m and the time sampling of the receiver field is 0.003 s. We apply a taper of 60 points at the lower and side boundaries of the model to minimize reflections from these boundaries. We perform forward modelling using a finite-difference code (Thorbecke and Draganov, 2011) in acoustic mode but with S-wave velocity parameters. This is justified, because in the field we generated and recorded SH waves, which decouple from the P and SV waves in a 2D experiment. To model SH-wave propagation assuming decoupling, one can thus use a simple acoustic forward modelling with S-wave velocities.

Figure 7b shows the stacked section obtained from the modelled CRSS data. Figure 7c shows the stacked section obtained from the retrieved common-source gathers after applying SI to the modelled CRSS data. In the stacking process, we use the RMS velocity field obtained from the exact velocity model. In the SI section, two clear bumps are visible at the first layer boundary with apex at the correct scatterer locations. In contrast, in the CRSS section the apex of the scatterers is not clear and the interpretation of the location of the scatterers is difficult because of the presence of large and strong diffraction smiles. If more scatterers were present (as in our field data), it would be difficult to distinguish the scatterers located at the layer boundary in the CRSS section. The diffraction smiles are nearly absent in the SI stacked section due to the improvement in stacking due to the increased fold of the traces to be stacked, because of more available sources and receivers. The top three layers are visible in both CRSS and SI sections. In the SI section, the layers are imaged well, except at the extremities of the receiver array. On the contrary, in the CRSS section the layers are clearly interpretable only at extremities of the receiver array where there is no interference due to the diffraction smiles. In the SI stacked section, the imaging of

To understand why the SI result could reveal scatterers that overlay reflectors, we perform a modelling study. We use a model consisting of four horizontal layers with two scatterers placed on the boundary between the two top layers (Figure 7a). The shear-wave velocity (V_s) and density (ρ) of the layers are: Layer1: V_s=82 m/s, ρ=800 kg/m^3; Layer 2: V_s=100 m/s, ρ=810 kg/m^3; Layer 3: V_s=120 m/s, ρ=820 kg/m^3; Layer 4: V_s=140 m/s, ρ=840 kg/m^3. Both scatterers are 1 m wide, 0.3 m high and have V_s=140 m/s and ρ=900 kg/m^3. The separation between the scatterers is 3 m. We consider the same acquisition geometry as we have in the field to generate synthetic data: 33 sources with 1 m spacing and 48 receivers with 0.5 m spacing. The first source is located at 134 m and the last source at 166 m, whereas the first receiver is located at 138 m and the last at 161.5 m. The scatterers are located at horizontal positions 148 m and 152 m. The grid sampling in the model is 0.09 m and the time sampling of the receiver field is 0.003 s. We apply a taper of 60 points at the lower and side boundaries of the model to minimize reflections from these boundaries. We perform forward modelling using a finite-difference code (Thorbecke and Draganov, 2011) in acoustic mode but with S-wave velocity parameters. This is justified, because in the field we generated and recorded SH waves, which decouple from the P and SV waves in a 2D experiment. To model SH-wave propagation assuming decoupling, one can thus use a simple acoustic forward modelling with S-wave velocities.

Figure 7b shows the stacked section obtained from the modelled CRSS data. Figure 7c shows the stacked section obtained from the retrieved common-source gathers after applying SI to the modelled CRSS data. In the stacking process, we use the RMS velocity field obtained from the exact velocity model. In the SI section, two clear bumps are visible at the first layer boundary with apex at the correct scatterer locations. In contrast, in the CRSS section the apex of the scatterers is not clear and the interpretation of the location of the scatterers is difficult because of the presence of large and strong diffraction smiles. If more scatterers were present (as in our field data), it would be difficult to distinguish the scatterers located at the layer boundary in the CRSS section. The diffraction smiles are nearly absent in the SI stacked section due to the improvement in stacking due to the increased fold of the traces to be stacked, because of more available sources and receivers. The top three layers are visible in both CRSS and SI sections. In the SI section, the layers are imaged well, except at the extremities of the receiver array. On the contrary, in the CRSS section the layers are clearly interpretable only at extremities of the receiver array where there is no interference due to the diffraction smiles. In the SI stacked section, the imaging of

reflections at the sides is poor due to insufficient stacking; the CMP fold is lower than that for the CRSS data. Note that the deepest reflector is not imaged in the SI data, because reflections from this boundary are not retrieved. This happens due to the length of the modelled data, which was sufficient to record the primary reflection from the fourth layer, but too short to record its free-surface multiples.

4.4 Remarks on the comparison of SI and CRSS results

From the comparison of CRSS and SI results in this section, the following remarks can be made:

- In the SI stacked section, scatterers appear at a time which is more likely to be the correct one, due to more available traces in the CMP gathers compared to the CRSS stacked section;
- Scatterers located at or close to a layer boundary are better imaged through SI;
- Shallow scatterers that are muted in the CRSS data can still be imaged in the SI stacked section.

However, as we found in our earlier modelling (Konstantaki et al., 2013), artifacts are also expected in the SI results. Therefore, a joint interpretation of CRSS and SI results is desirable in order to interpret correctly the scatterers.

5. REMOVING SURFACE WAVES USING SEISMIC INTERFEROMETRY: IMPROVED IMAGING OF THE REFLECTORS IN A LANDFILL

5.1 Preparation of data for adaptive subtraction

Surface waves with velocity and frequency similar to those of the reflections and the scattering events are present in our field data and it is challenging to remove them through data processing. In the processing of CRSS data we remove the surface waves by surgical muting. This does not remove the surface-wave energy in a satisfactory manner, because the surface-wave energy that overlaps the useful reflection and scattered arrivals still stays. Furthermore, weak reflections and scattered arrivals covered by surface waves can also be muted.

Here, we use SI as a tool to remove in a data-driven way the surface-wave energy from the shallow reflection data. For this purpose, we subtract the surface waves in an adaptive manner. To remove the surface waves from the CRSS data, first we need to predict the surface waves by retrieving them with SI. We first compensate for the intrinsic loss by multiplying the CRSS data with $\exp(1.3*t)$. Then, we apply a bandreject

filter (5-35-95-110 Hz) followed by top muting of the direct arrivals in order to enhance the surface waves. Note that we now apply a bandreject filter to reject frequencies that were kept before (those characteristic of reflections and diffractions) and boost low and high-frequency surface waves (that were rejected during the SI and CRSS processing). After that, we apply SI using the mixed-traces approach as explained in section 3. The result is SI data with dominant surface waves (SI^S).

An example of this retrieval in field data is illustrated in Figure 8b. For a comparison, the CRSS shot gather at the same location (shot at 22 m horizontal distance) is shown in Figure 8a. Next, we use a least-squares matching filter that minimizes the difference between the CRSS and the SI^S data (Verschuur et al., 1992; Guitton and Verschuur, 2004). For our data, we found that the best matching is achieved when we use a filter with a length of 21 sample points, a time window of 100 sample points, and a spatial window of 5 traces. Using this filter, the SI^S data (Figure 8b) are adaptively subtracted from the CRSS data (Figure 8a). The resulting AS data is shown in Figure 8c.

5.2 Comparison of the results of CRSS and AS

Comparing the gathers in Figures 8a and 8c, we see that surface-wave energy is significantly removed, and at many places the reflections are better identifiable in the AS shot gather. Refractions, now free from surface-wave energy, are also better visible. In Figure 8b, the SI^S shot gather shows an event at about 16 m horizontal distance and TWT of 0 ms, which looks like a surface wave from another source. This event is also present in the CRSS data and becomes clearly visible when the same bandpass filter is applied. Figures 9a and 9b show the shot gathers from Figures 8a and 8c, respectively, after top and bottom muting. We apply the same top and bottom mute in both shot gathers. The application of SI followed by AS suppresses very effectively the surface waves at later times. In our case, for imaging the landfill using shear waves, we are mainly interested in the first 180 to 200 ms (which corresponds to approximately 11 to 13 m depth where we expect the bottom of the landfill). Therefore, for comparison, we apply the same bottom mute as that for the CRSS data. Note that in the AS data we do not apply surgical mute to all shot gathers for surface-wave removal - only a few shot gathers show remaining strong surface waves that need to be removed by surgical muting. This is because the AS filter parameters are not ideal for all shot gathers and in a number of shot gathers a few surface waves are still present. The grey-shaded areas in Figures 9a and 9b highlight reflections from layer boundaries. The red hyperbolas highlight the scattering events interpreted on the CRSS data (Figures 4a and 9a), whereas the green hyperbolas are the scattering

events interpreted on the SI data (Figure 4d). The reflections (grey-shaded areas) are identifiable in the AS result – some of them are even more continuous and laterally coherent. The scattering events are not improved after AS, but this is also not expected. The quality of the scatterers might even have deteriorated.

During the SI processing, surface waves between a virtual source and a receiver are retrieved for each of the active-source positions, over which the summation takes place. This results in a retrieval of relatively strong surface waves. A reflection between the same virtual source and a receiver will be retrieved only for a few sources, which lie in the stationary-phase region. Because of this, the retrieved reflections will be relatively weak unless a large number of sources are available. Scattered arrivals between the virtual sources and the receiver might also be retrieved for each active-source position, but that will depend on the recording time and the path of the scattered wave in the CRSS data. Because of this, a retrieved scattering will be relatively stronger than a retrieved reflection, but relatively weaker than a retrieved surface wave. In the AS, the strongest arrivals, i.e. the surface waves, will dictate the parameters of the matched filter and thus the surface waves will be most effectively removed. The weaker arrivals, like the scattering, might also be affected, but to a lesser extent. How much of the scattered energy is preserved after the AS would depend on how much surface-wave energy is retrieved and the difference in amplitude between the surface waves and the scattered arrivals.

Figure 10 shows the stacked sections from the CRSS and AS data. Note that in the AS section the reflectors are clearer. The interpretations are marked in Figures 10c and 10d. The grey-shaded areas highlight the reflectors. The reflectors on the right and left sides (18 m to 26.25 m and 5.25 m to 8 m horizontal distance, respectively) are more continuous in the AS result. On the other hand, between about 12 m and 15 m horizontal distance, TWT of 140 ms the reflectors appear to be more continuous in the CRSS data. The reason for this is likely to be the surface-wave energy that was not removed in the AS data, but was removed in the CRSS data by surgical muting. Note that the AS section allows much better identification of the bottom of the landfill (yellow line in Figure 10d).

As discussed earlier, the scatterers in the AS section in Figure 10 are not always well-imaged as compared with the CRSS section. The scatterers highlighted with red hyperbolas are imaged satisfactorily, although not always at the same location as in the CRSS data. The green-highlighted scatterers are difficult to interpret.

Ideally, SI can be applied to the AS data to improve the retrieval of scattering events compared to the original SI data (SI applied directly to the CRSS), since the

interference from surface-wave energy would be less in case of the AS data. However, our field data have a low S/N, implying that SI applied to the CRSS data would also result in a low S/N and consequently the AS result has a lower S/N. The application of SI on the result of AS would be even worse. To improve the retrieval of the scattered arrivals, one needs to have longer AS data. If the noise in the field data can be reduced through more careful data acquisition, then that will help the situation greatly.

6. CHARACTERIZATION

For a reliable estimation of the emission potential of a landfill, determination of the detailed density distribution is important (White et al., 2004; McDougall and Fleming, 2013). Konstantaki et al. (2015) translated the velocity field obtained from CRSS data to density distribution using a tested empirical relationship that is specifically valid for landfill sites. Errors in the velocity models, however, significantly influence the characterization of the landfill properties (e.g., Zhu et al., 1998). Therefore, the extracted velocity field needs to be reliable.

As we have shown above, CRSS may fail to image certain scatterers and reflectors, whereas using SI one might improve the imaging of the shallow subsurface. However, SI might also create artifacts. Therefore, a combined interpretation of the velocity fields obtained from CRSS, SI and AS might lead to a more reliable characterization of the shallow subsurface.

For all three datasets (CRSS, SI and AS), we estimate the RMS velocities by interactive velocity analysis. For this, we follow the procedure specifically valid for a very heterogeneous subsurface condition like in landfills, as explained in Konstantaki et al. (2015). This requires special care. Using the Dix equation, we then convert the RMS velocities to interval velocities. Figures 11a,b,c illustrate the estimated velocity field obtained from the CRSS, SI, and AS data, respectively. The circles in Figure 11 mark areas showing clear differences among the three velocity fields. The SI data present a more heterogeneous velocity field compared to the AS data. This is anticipated because SI illuminates multitude of localized scatterers in the landfill. On the other hand, the AS velocity field is smoother, because of the predominance of reflections from layer boundaries rather than from spatially localized scatterers. The differences between the three velocity fields appear meaningful.

These differences can be explained based on the events that each dataset (CRSS, SI and AS) images. We present a few examples here. In the CRSS data in Figure 5c, a scatterer is imaged at about 8.5 m horizontal distance and TWT of 150 ms (red

hyperbola). This scatterer appears in the CMP gathers, and during the velocity analysis, velocity was picked such that this scatterer is imaged best (Konstantaki et al., 2015). For this reason, a high-velocity anomaly compared to the surrounding appears at this location (marked by A in Figure 11a). On the other hand, in the SI data, not one but two scatterers are imaged in this vicinity (Figure 5d): 8.75 m horizontal distance and TWT of 130 ms, and 9.25 m horizontal distance and TWT of 100 ms (green hyperbolas), although no scatterer is imaged at exactly the same location marked by the red hyperbola (scatterer in the CRSS data). This is the reason why we notice in the SI velocity field two spatially resolved high-velocity localities (marked by two circles close to A). At location B, a lower velocity appears in the SI velocity field compared to the CRSS velocity field. This is because a scatterer is imaged at this location in the SI data (see the SI stacked section in Figure 5d at 9.25 m horizontal distance and TWT of 25 ms), but not in the CRSS data (Figure 5c). Next, the velocity contrast at location C appears at different times between Figures 11a and 11b, because of the opposite-polarity effect. As discussed in section 4.2, the scatterer at around 16 m horizontal distance in the CRSS stacked section (Figure 5c yellow rectangle, red hyperbola) appears at a later time than that in the SI stacked section (Figure 5d yellow rectangle, green hyperbola). Because of this, we find the velocity contrast appearing at a later time in the SI velocity field (Figure 11b) compared to the CRSS velocity field (Figure 11a). SI fails to image the scatterer located at about 25.75 m horizontal distance and TWT of 150 ms (Figure 5d), which is though clearly visible in the CRSS data (Figure 5c). This explains the presence of a clear anomaly at this location in the CRSS velocity field and its absence in the SI velocity field (circle D).

Compared to the CRSS and SI velocity fields, the AS velocity field is generally rather smooth (dominated by reflections from the layer boundaries rather than by the scatterers). Nevertheless, a few localized velocity contrasts can be traced in Figure 11c. As discussed earlier, several scatterers are still picked in the AS data during velocity analysis, and they are imaged in the AS stacked section. We, therefore, still observe some spatially localized velocity anomalies in Figure 11c. Circle A in this figure indicates a localized scatterer in this area (corresponds to the one at 8.5 m to 9.25 m horizontal distance and TWT of 100 ms to 150 ms in Figure 10d). Similarly, circle C in Figure 11c indicates the velocity anomaly due to scatterers at approximately 16 m distance and TWT of 100 ms and 130 ms (Figure 10d). Admittedly, in the AS stacked section, due to the lower S/N, the imaged scatterers are sometimes less unambiguous, as explained in the previous section. Therefore, one needs to be cautious in interpreting the localized anomalies in the AS velocity field.

7. DISCUSSION

In the SI stacked section we observe a dome-like structure with a peak at around 13 m to 17 m horizontal distance (Figure 5b). Indication of such a structure is faint in the CRSS section (Figure 5a). This structure is due to stacking of the surface waves that remained after top muting. The following reasons support this interpretation. First, compared to the raw CRSS shot gathers, reverberating surface waves are accentuated in the raw shot gathers obtained from SI applied to the CRSS data (Figure 4). After top muting, the surface waves are still present more in the SI shot gathers than in the CRSS shot gathers, and these surface waves stack up to produce this dome-like structure, more prominently in the SI stacked section than in the CRSS stacked section. Second, when the surface waves in the CRSS data are greatly suppressed by adaptive subtraction, the stacked section shows no more indication of such dome-like structure (Figure 10b). Third, the frequency content of the dome structure is relatively low and suggestive of ground rolls (see also Figures 4b, 4d and 8b). Finally, in our data acquisition, the geophones were fixed and only the source moved. The CMP fold reaches its maximum at 13.5 m lateral distance and then stays constant at 24 m till 18.25 m lateral distance for the CRSS data, whereas it reaches a maximum of 48 traces at 15.75 m for the SI data. On both sides of this distance range, the fold gradually decreases (Figure 5). Note that the peak of the dome-like structure is located around 13-17 m distance range (Figure 5b). Both positive and negative offsets in the CMP gather contain the remaining surface waves which stack up at an earlier time. Outside this lateral distance range, the positive and negative offsets are not equal and this inequality increases as we go farther from the above distance range. Accordingly, the result of stacking of the remaining surface waves in the positive and negative offsets gradually changes to create the flank of the dome-like structure.

Such a dome-like structural artefact due to stacking of surface waves can be avoided in case the data are acquired using the usual roll-along spread. Then the maximum CMP fold and distribution of source-receiver offset will remain constant over many CMPs. But in that case, the surface waves will stack up to produce an artifact which will appear like a flat, laterally continuous reflector. Because the reverberating surface waves are stronger in the SI data, this is more of a problem in case of SI imaging. Our results indicate that precaution is needed during acquisition and interpretation, in case SI is applied to CRSS data. The strong reverberation of surface waves in case of SI is possibly due to the limitation in the available frequency bandwidth and/or the very near-surface scattering.

If a scatterer is present very close to the surface, SI will reveal its presence through retrieval of an event with opposite (positive and negative) linear moveouts at a place of no virtual source. Such an event is visible in Figure 8b close to time zero at approximately 16 m lateral distance. This scatterer will also be imaged in the stacked section, if the event is not suppressed during NMO stacking targeted at imaging the layer boundaries. Additionally, the increased stacking power of SI will make this event stronger compared to CRSS section. In CMP stacking we use the RMS velocity field corresponding to the continuous reflection horizons, and as a result the scatterers are not flattened. As the SI data have a higher number of traces compared to the CRSS data, the imaging of the apex of the scatterers is improved in the SI stacked sections, which was also illustrated in Konstantaki et al. (2013).

We use a trace-stacking procedure for imaging after application of SI. This accounts for single scattering. When multiple scattering is present, then the imaging in depth can be improved using advanced imaging conditions incorporated in prestack depth migration (Fleury and Vasconcelos, 2012; Vasconcelos et al., 2012; Ravasi and Curtis, 2013). In addition, we use 2D approximation for the seismic imaging of the scatterers. However, signals from scatterers located in the 3D surrounding of our line are also recorded. Thus, some of the scatterers we are imaging might not be exactly situated under our 2D seismic line. On the other hand, scattering from the 3D environment helps to illuminate our receivers better and thus aids in suppressing artifacts. For the AS results, the presence of 3D ambient noise can be an explanation why the filter did not sufficiently remove all surface-wave energy.

8. CONCLUSIONS

We studied the application of seismic interferometry (SI) to the conventional reflection seismic survey (CRSS) field data obtained at a landfill, with the goal to improve the imaging and interpretation of the landfill heterogeneities. We have shown that SI applied to the CRSS data improves the imaging of scatterers inside the landfill. We have also shown that scatterers that are located on or close to a layer interface might not be imaged using the CRSS data, but can be imaged using the retrieved SI data. Due to the coarser spatial sampling of the source in the CRSS data, the scatterers might be imaged at a slightly later time/depth. Because the SI-retrieved data have a denser spatial sampling, the chance of imaging the scatterers at their correct time/depth is greater. During the processing of CRSS data, muting of the earlier times might cause shallower scatterers not to be imaged. Such scatterers would still be

imaged using the SI-retrieved data. We investigated the efficiency of SI surface-wave prediction and adaptive subtraction from the original CRSS data on landfill. We showed that the obtained adaptively-subtracted (AS) data result in an improved image of the reflectors inside the landfill body. The integrated interpretation of the CRSS, SI and AS data improved the understanding of the landfill's subsurface. The three velocity fields provide complementary information and they may help distinguish the high-density areas that are responsible for the preferential flow paths that occur inside a landfill. This can provide useful information for designing the treatment technologies, for the prediction of the emission potentials, and for assessing the temporal changes in the landfill body.

ACKNOWLEDGEMENTS

REFERENCES

Brouwer J., Ghose R., Helbig K. and Nijhof V., 1997. The improvement of geotechnical subsurface models through the application of S-wave reflection seismic exploration. 3rd Annual Meeting, EEGS, Extended Abstracts, 103-106.

Campillo M. and Paul A., 2003. Long-range correlations in the diffuse seismic coda. Science 299. doi:10.1126/science.1078551

Dong S., He R. and Schuster T., 2006. Interferometric prediction and least-squares subtraction of surface waves. SEG Technical Program Expanded Abstracts 2006, 2783-2786.

Draganov D., Wapenaar C.P.A., Mulder W., Singer J. and Verdel A., 2007. Retrieval of reflections from seismic background-noise measurements. Geophysical Research Letters 34. doi:10.1029/2006GL028735

Draganov D., Campman X., Thorbecke J., Verdel A. and Wapenaar C.P.A., 2009. Reflection images from ambient seismic noise. Geophysics 74, A63-A67. doi:10.1190/1.3193529

Draganov D., Heller K. and Ghose R., 2012. Monitoring CO_2 storage using ghost reflections retrieved from seismic interferometry. International Journal of Greenhouse Gas Control 11S, S35-S46. doi:10.1016/j.ijggc.2012.07.026

Fleury C. and Vasconcelos I., 2012. Imaging condition for nonlinear scattering-based imaging. Estimate of power loss in scattering. Geophysics 77, S1-S18. doi:10.1190/geo2011-0135.1

Ghose R., 2002. High-frequency shear wave reflections from shallow subsoil layers using a vibrator source: Sweep cross-correlation versus deconvolution with groundforce derivative. 72nd Annual International Meeting, SEG, Expanded Abstracts, 1408-1411.

Ghose R., 2003. High-frequency shear-wave reflections to monitor lateral variations in soil, supplementing downhole geotecnhical test, in: J. Saveur (Ed.), Reclaiming the Underground Space. Proc. ITA World Tunneling Congress, Amsterdam, The Netherlands, Swets & Zeitlinger, Lisse, 827-833.

Ghose R., 2012. A microelectromechanical system digital 3C array seismic cone penetrometer. Geophysics 77, WA99-WA107. doi:10.1190/GEO2011-0266.1

Ghose R., Brouwer J. and Nijhof V., 1996. A portable S-wave vibrator for high-resolution imaging of the shallow subsurface. 58th Annual International Conference and Exposition, EAGE, Extended Abstracts, M037.

Ghose R., Nijhof V., Brouwer J., Matsubara Y., Kaida Y. and Takahashi T., 1998. Shallow to very shallow, high-resolution reflection seismic using a portable vibrator system. Geophysics 63, 1048-1056. doi:10.1190/1.444798

Ghose R. and Goudswaard J., 2004. Integrating S-wave seismic reflection data and cone-penetration-test data using a multiangle multiscale approach. Geophysics 69, 440-459. doi:10.1190/1.1707064

Guitton A. and Verschuur D.J., 2004. Adaptive subtraction of multiples using the L_1-norm. Geophysical Prospecting 52, 27-38. doi:10.1046/j.1365-2478.2004.00401.x

Halliday D.F., Curtis A., Robertsson O.A. and van Manen D.-J., 2007. Interferometric surface wave isolation and removal. Geophysics 72, A69-A73. doi:10.1190/1.2761967

Halliday D.F., Curtis A., Vermeer P., Strobbia C., Glushchenko A., van Manen D.-J. and Robertsson O.A., 2010. Interferometric ground-roll removal: Attenuation of

scattered surface waves in single-sensor data. Geophysics 75, SA15-SA25. doi:10.1190/1.3360948

King S. and Curtis A., 2012. Suppressing nonphysical reflections in Green's function estimates using source-receiver interferometry. Geophysics 77, Q15-Q25. doi:10.1190/geo2011-0300.1

Konstantaki L.A., Draganov D., Heimovaara T. and Ghose R., 2013. Imaging scatterers in landfills using seismic interferometry. Geophysics 78, 1-10. doi:10.1190/GEO2013-0099.1

Konstantaki L.A., Ghose R., Draganov D., Diaferia G. and Heimovaara T., 2015. Characterization of a heterogeneous landfill using seismic and electrical resistivity data. Geophysics 80, 1-13, doi:10.1190/GEO2014-0263.1

McDougall J.R. and Fleming I.R., 2013. Hydro-bio-mechanical modelling of filling and post closure landfill behaviour - a case study. HPM5 Fifth international workshop on hydro-physico-mechanics of landfills, Edinburgh, 77-88.

Ravasi M. and Curtis A., 2013. Nonlinear scattering based imaging in elastic media: Theory, theorems and imaging conditions. Geophysics 78, S137-S155. doi:10.1190/geo2012-0286.1

Scharff H., 2005. Ideas and intentions of the Dutch sustainable landfill research program. Presented at the International Seminar and Workshop "The Sustainable Landfilling" Abbey of Praglia, Padua, Italy.

Schuster G.T., 2001. Theory of daylight interferometric imaging: Tutorial. 63rd Annual International Conference and Exhibition, EAGE, Extended Abstracts, A32.

Schuster G.T., Yu J., Sheng J. and Rickett J., 2004. Interferometric/daylight seismic imaging. Geophysical Journal International 157, 838-852. doi:10.1111/j.1365-246X.2004.02251.x

Shapiro N.M. and Campillo M., 2004. Emergence of broadband Raleigh waves from correlations of the ambient seismic noise. Geophysical Research Letters 31, L07614. doi:10.1029/2004GL019491

Snieder R., 2004. Extracting the Green's function from the correlation of coda waves: A derivation based on stationary phase. Physical Review E 69, 0466610, doi: 10.1103/PhysRevE.69.046610

Snieder R., Wapenaar C.P.A. and Larner K., 2006. Spurious multiples in seismic interferometry of primaries. Geophysics 71, SI111-SI124. doi:10.1190/1.2211507

Thorbecke J. and Draganov D., 2011. Finite-difference modeling experiments for seismic interferometry. Geophysics 76, H1-H18. doi:10.1190/geo2010-0039.1

van Manen D.-J., Robertsson O.A. and Curtis A., 2005. Modeling of wave propagation in inhomogeneous media. Physical Review Letters 94, 164301, doi:10.1103/PhysRevLett.94.164301

van Vossen W.J., 2010. Sustainable landfilling in the Netherlands: developments, methodologies and experiences. Österreichische Wasser- und Abfallwirtschaft 62, 141-148. doi:10.1007/s00506-010-0201-6

van Wijk K., 2006. On estimating the impulse response between receivers in a controlled ultrasonic experiment. Geophysics 71, S179-S184.

Vasconcelos I., Robertsson J., Vassalo M. and van Manen D.-J., 2012. Reverse-time imaging of dual-source 4C marine seismic data using primaries, ghosts and multiples. 74th Annual Conference and Exhibition, EAGE, Extended Abstracts, X045.

Verschuur D.J., Berkhout A.J. and Wapenaar C.P.A., 1992. Adaptive surface-related multiple elimination. Geophysics 57, 1166-1177. doi:10.1190/1.1443330

Wapenaar C.P.A., 2004. Retrieving the elastodynamic Green's function of an arbitrary inhomogeneous medium by cross correlation. Physical Review Letters 93, 254301. doi:10.1103/PhysRevLett.93.254301

Wapenaar C.P.A., 2006. Green's function retrieval by cross-correlation in case of one-sided illumination. Geophysical Research Letters 33, L19304. doi:10.1029/2006GL027747.

Wapenaar C.P.A., Draganov D., Thorbecke J. and Fokkema J.T., 2002. Theory of acoustic daylight imaging revisited. 72nd Annual International Meeting, SEG, Expanded Abstracts, 2269-2272.

Wapenaar C.P.A. and Fokkema J., 2006. Green's function representations for seismic interferometry. Geophysics 71, SI33-S146. doi:10.1190/1.2213955

Wapenaar C.P.A., Draganov, D., Snieder, R., Campman, X. and Verdel, A., 2010a. Tutorial on seismic interferometry: Part 1 - Basic principles and applications. Geophysics 75, 75A195-75A209, doi:10.1190/1.3457445

Wapenaar C.P.A., Slob E., Snieder R. and Curtis A., 2010b. Tutorial on seismic interferometry: Part 2 - Underlying theory and new advances. Geophysics 75, 75A211-75A227. doi:10.1190/1.3463440

White J.K., Robinson J. and Ren Q., 2004. Modelling the biochemical degradation of solid waste in landfills. Waste Management 24, 227-240. doi:10.1016/j.wasman.2003.11.009

Zhu J., Lines L.R. and Gray S.H., 1998. Smiles and frowns in migration/velocity analysis. Geophysics 63, 1200-1209. doi:10.1190/1.1444420
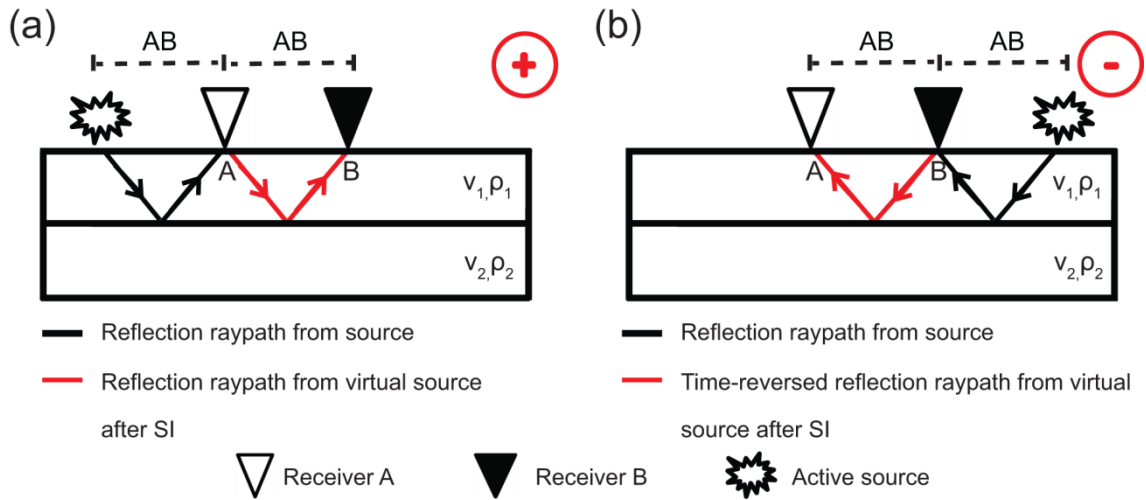
Figure 1: Explanation of retrieval of a reflection at B from a virtual source at A. The active source is at distance AB from A or from B. (a) When the active source is to the left of A, the reflection is retrieved at positive times. (b) When the active source is to the right of B, the reflection would be retrieved at negative times. The symbols v and ρ denote velocity and density, respectively.
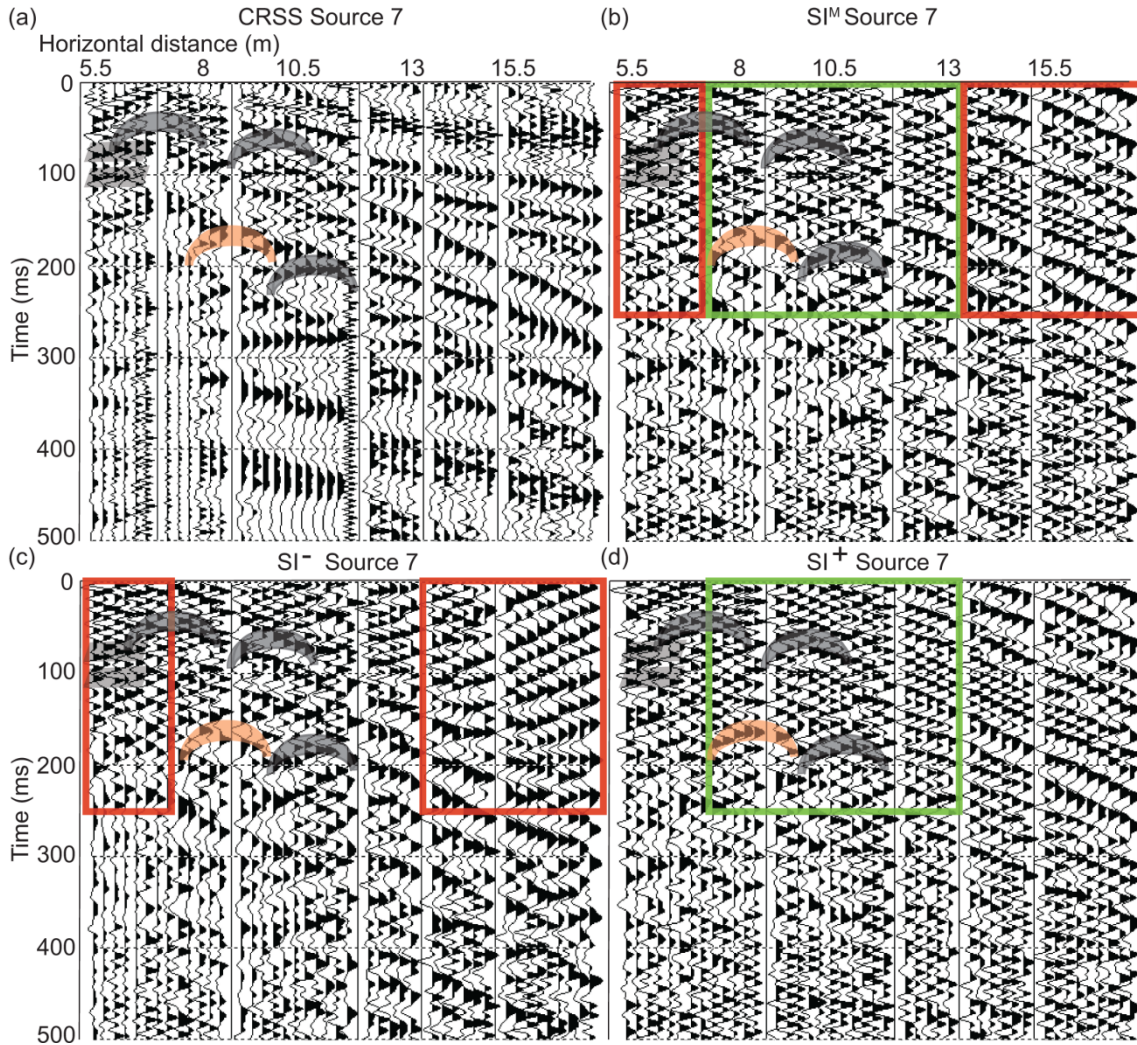
Figure 2: Raw shot gather for a source located at horizontal distance 7 m, obtained from (a) conventional reflection seismic survey (CRSS), (b) seismic interferometry (SI) using the mixed-traces approach (SI^M), (c) SI taking only the negative times (SI$^-$), and (d) SI taking only the positive times (SI$^+$). The green rectangle shows areas of improvement in SI^M over SI$^+$, the red rectangles show areas of improvement in SI^M over SI$^-$. The grey-shaded areas and hyperbolas show reflection and scattering events, respectively. The orange hyperbola indicates an artifact in SI$^+$. Note that we apply a different bandpass filter to the SI results (Figures 2b,c,d) compared to the CRSS result (Figure 2a).
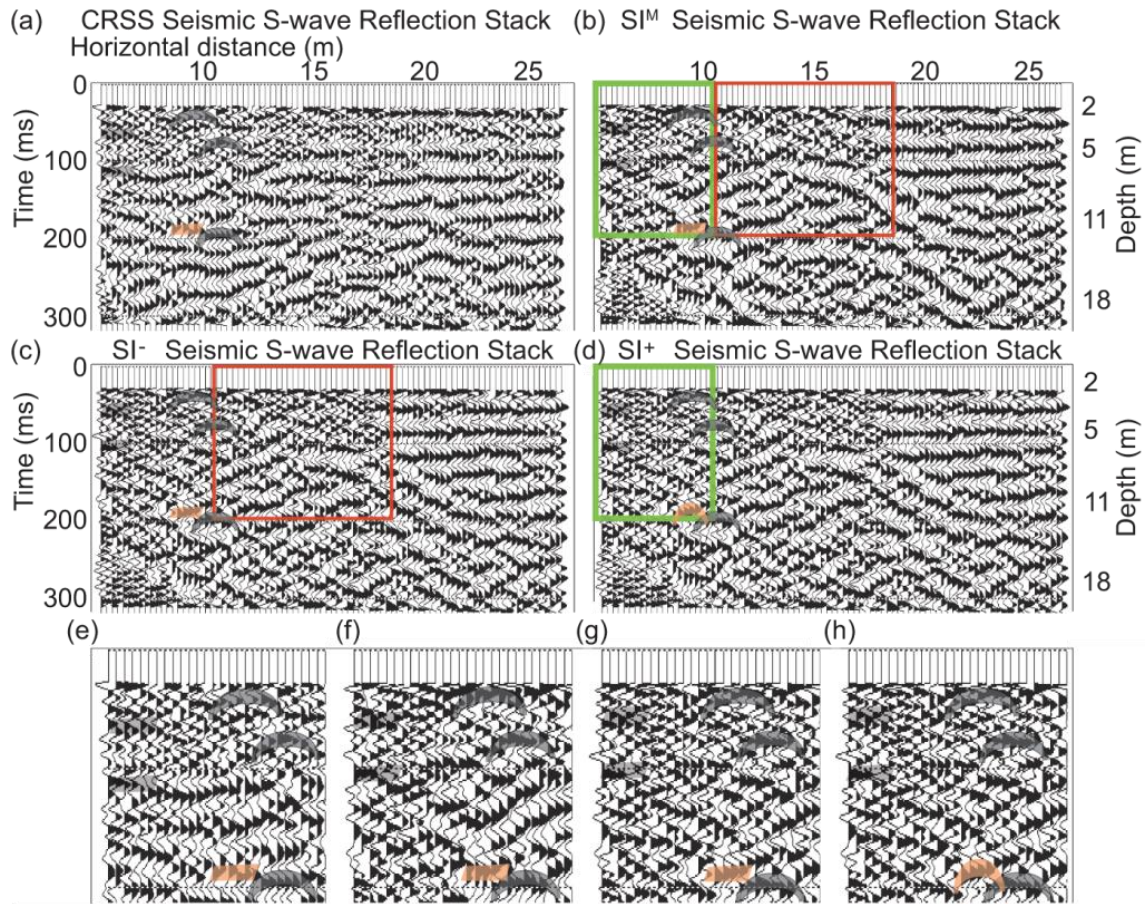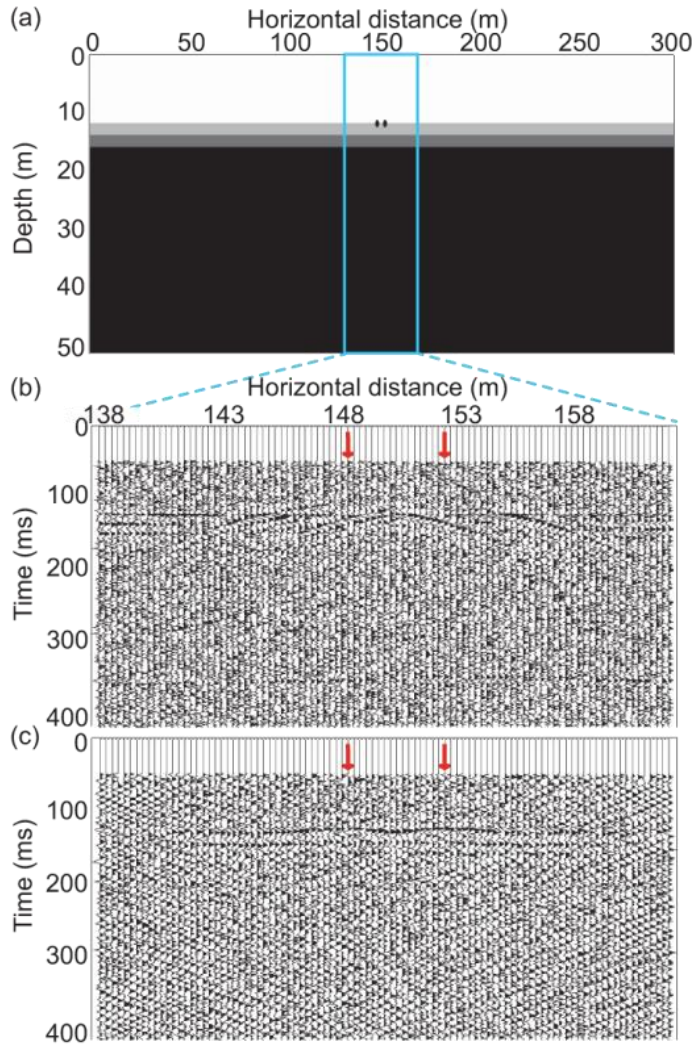
Figure 3: Stacked section obtained from (a) conventional reflection seismic survey (CRSS), (b) seismic interferometry (SI) using the mixed-traces approach (SI^M), (c), SI taking only the negative times (SI$^-$) and, (d) SI taking only the positive times (SI$^+$). (e) enlarged area showing the scatterers in (a), (f) enlarged area showing the scatterers in (b), (g) enlarged area showing the scatterers in (c), (h) enlarged area showing the scatterers in (d). The green rectangle shows the area of improvement in SI^M over SI$^+$, the red rectangle shows the area of improvement of SI^M over SI$^-$. The grey-shaded areas and hyperbolas mark some reflections and scatterers, respectively. The orange hyperbola indicates an artifact in SI$^+$. The dome-like structure in the middle, accentuated in the SI sections, is due to the remaining surface waves and the laterally varying positive and negative offsets due to split-spread data acquisition with a fixed receiver array, which will be explained further in the Discussion section.
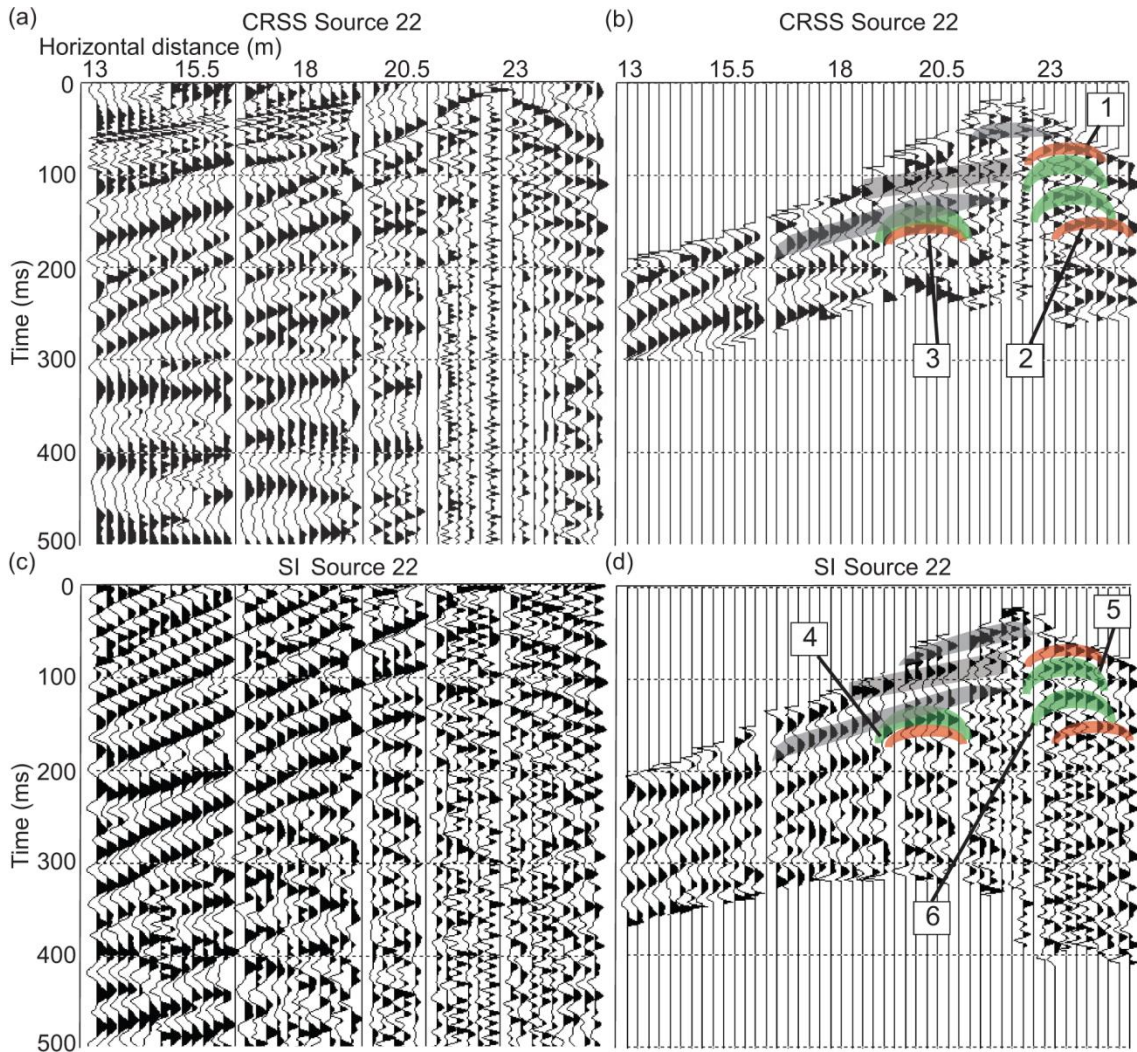
Figure 4: (a) Raw and (b) processed shot gather obtained from conventional reflection seismic survey (CRSS) for a source located at horizontal distance 22 m. (c) Raw and (d) processed shot gather obtained from seismic interferometry (SI) applied to the CRSS data, for a virtual source located at horizontal distance 22 m. The red hyperbolas show scattering events interpreted on the CRSS data, whereas the green hyperbolas mark scattering events interpreted on the SI data. The grey-shaded areas indicate mostly reflections.
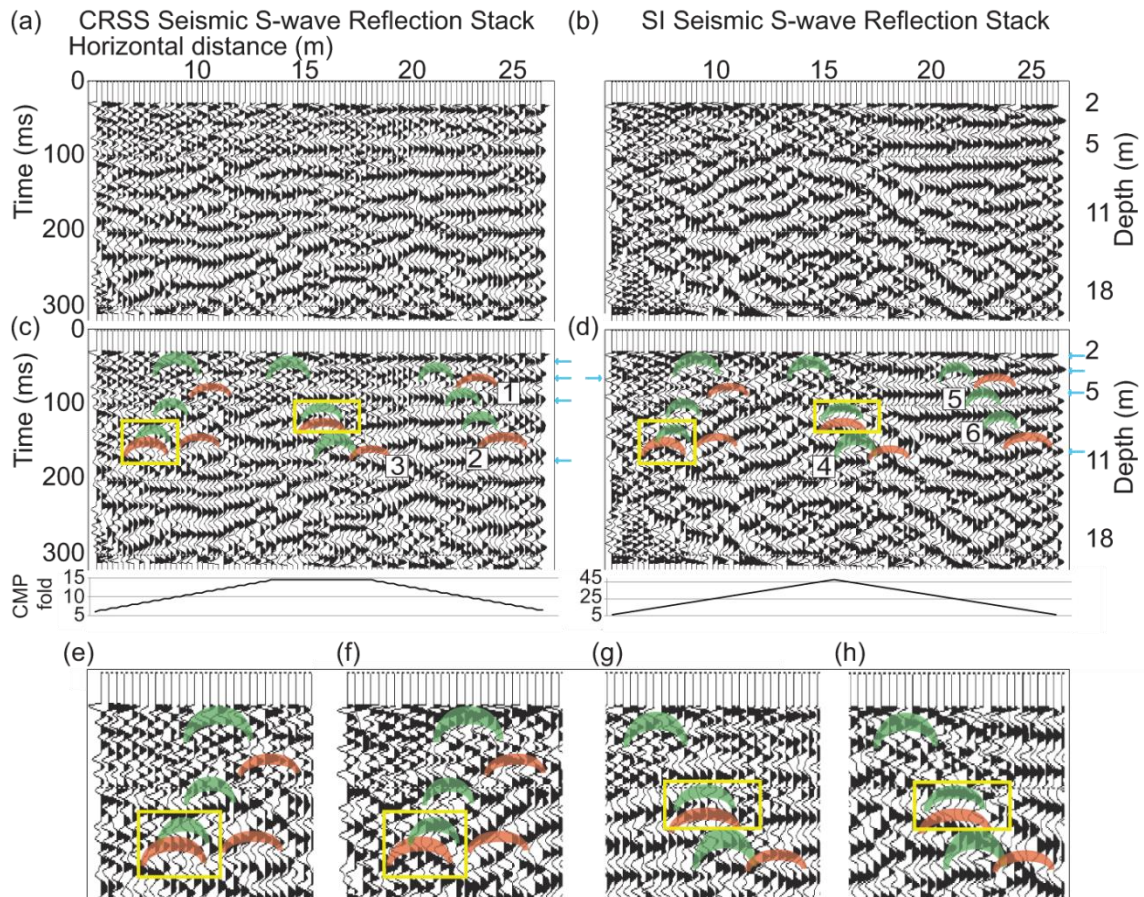
Figure 5: Stacked section obtained from (a) conventional reflection seismic survey (CRSS) and, (b) seismic interferometry (SI) with the mixed-traces approach applied to the CRSS data. (c) and (d) show the interpretation from (a) and (b), respectively, (e) enlarged area showing the scatterers in the left side of (c), (f) enlarged area showing the scatterers in the left side of (d), (g) enlarged area showing the scatterers in the middle of (c), (h) enlarged area showing the scatterers in the middle of (d). The red hyperbolas show scatterers interpreted on the CRSS data, whereas the green hyperbolas show scatterers interpreted on the SI data. The numbers correspond to the scattering events shown in Figure 4. The yellow rectangles illustrate examples of opposite-polarity effect. The blue arrows point to reflectors. The CMP fold distribution is shown in the lower part. Note that the peak of the dome-like structure, more prominent in the SI reflection stack (b), is located in the lateral distance range which corresponds to the maximum CMP fold.
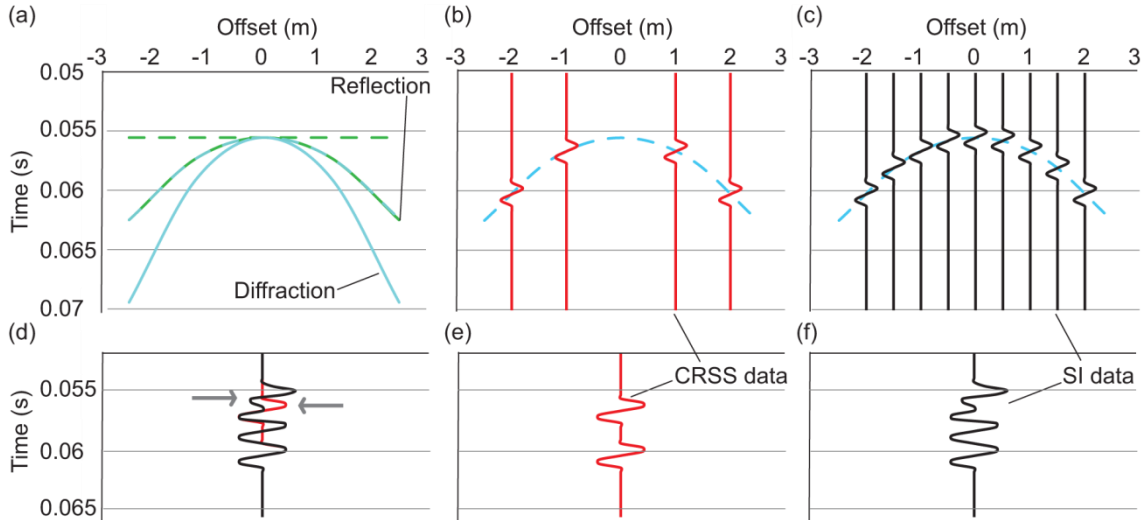
Figure 6: (a) Reflection and diffraction hyperbolas (solid lines) and their alignment after normal moveout (NMO) correction (dashed lines) using the root-mean square velocity of the reflection event. (b) Diffraction event in the common-midpoint (CMP) gather of conventional reflection seismic survey (CRSS) and, (c) diffraction event in the CMP gather of seismic interferometry (SI). (d) Comparison of stacked CRSS (red) and SI (black) traces, (e) stacked CRSS trace only, (f) stacked SI trace only. The grey arrows in (d) mark the opposite-polarity effect.

Figure 7: (a) Velocity model for forward modelling of a situation where two scatterers are located at the boundary between the two layers. Synthetic stacked section obtained using the (b) conventional reflection seismic survey (CRSS) data and (c) data retrieved by application of seismic interferometry to the CRSS data. The red arrows indicate the location of the scatterers.
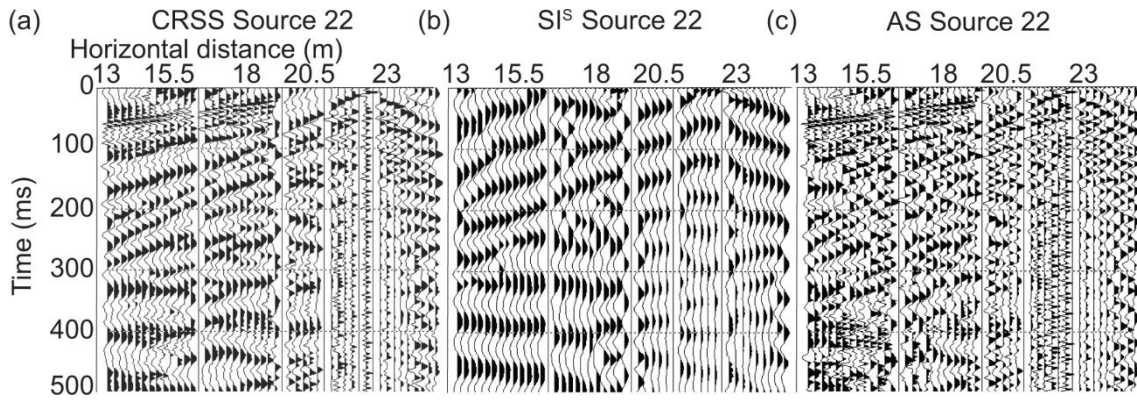
Figure 8: Shot gather for source located at horizontal distance 22 m obtained from (a) conventional reflection seismic survey (CRSS), (b) seismic interferometry focused towards retrieving primarily the surface waves, and (c) CRSS after adaptive subtraction of the retrieved surface waves, which is the subtraction of the gather in (b) from that in (a).
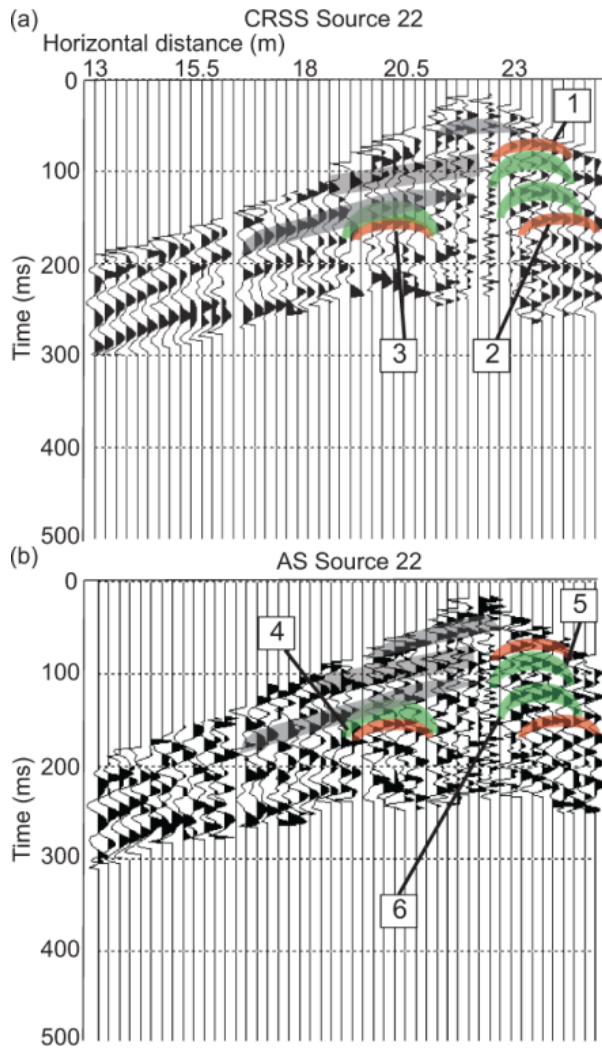
Figure 9: The shot gather (a) from Figure 8a and (b) from Figure 8c after processing (top and bottom muting). The red hyperbolas show the scattering events interpreted on CRSS data, whereas the green hyperbolas mark the same events interpreted on the SI data. The grey-shaded areas indicate primarily reflections.
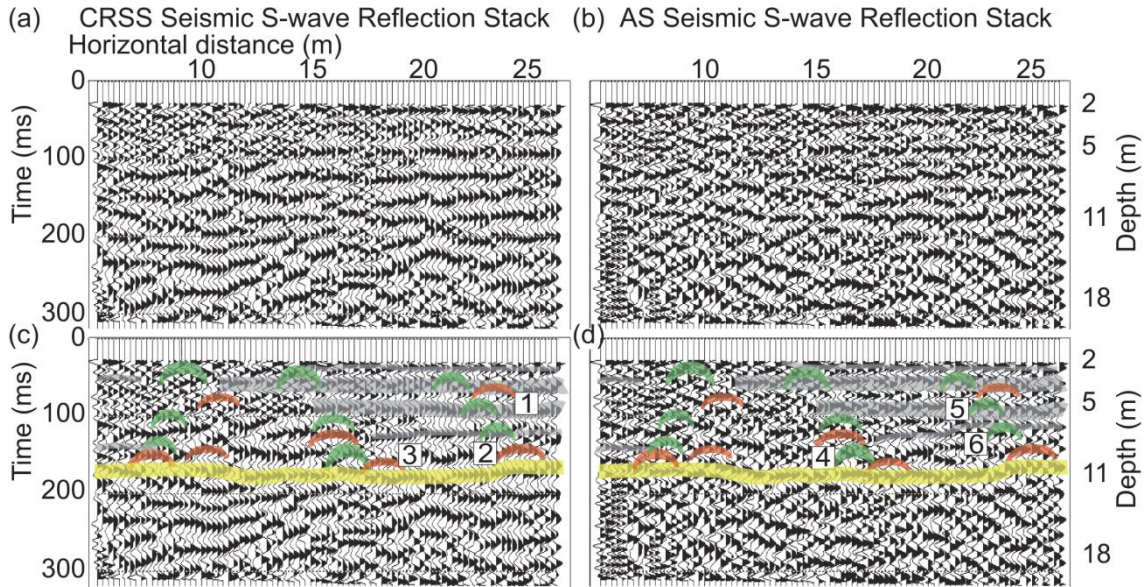
Figure 10: Stacked section obtained from (a) conventional reflection seismic survey (CRSS) and, (b) adaptive subtraction (AS) of surface waves. Interpreted stacked section (c) of CRSS and (d) of AS. The red hyperbolas indicate scatterers interpreted on the CRSS data, whereas the green hyperbolas indicate scatterers interpreted on the SI data. The numbers correspond to scattering events shown in Figure 9. The grey-shaded areas indicate reflectors (layer boundaries). The yellow line indicates the interpreted landfill bottom.
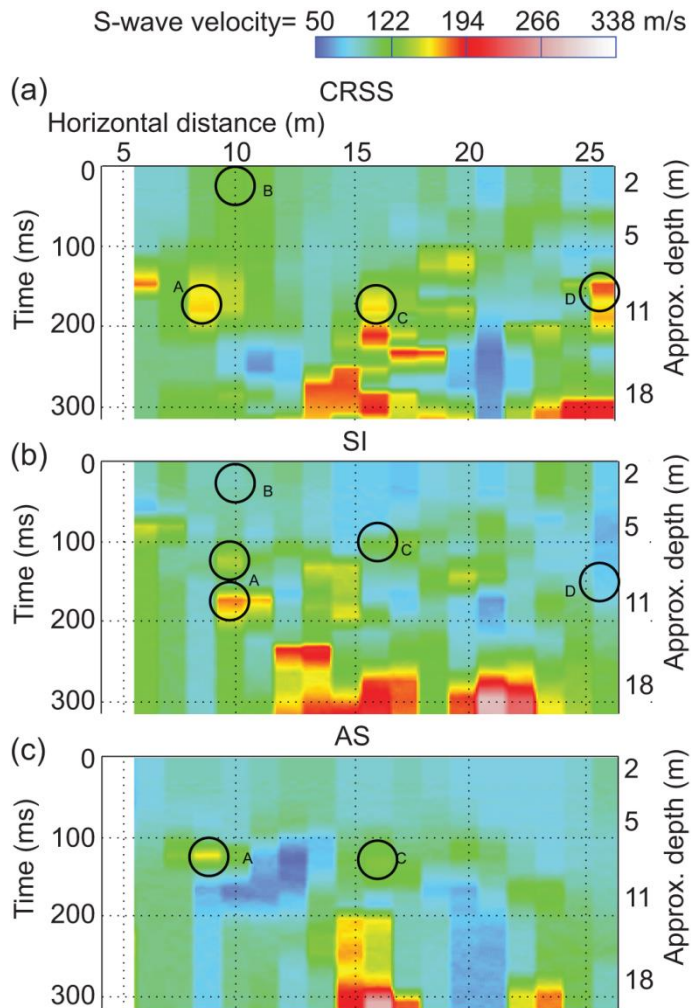
Figure 11: S-wave interval velocity field obtained from (a) conventional reflection seismic survey (CRSS) data, (b) seismic interferometry (SI) data and, (c) data after adaptive subtraction (AS) of surface waves. The circles and capital letters indicate areas where differences in the velocity fields among the three fields are observed.